

Article

Synergetic Effects of Mixed-Metal Polyoxometalates@Carbon-Based Composites as Electrocatalysts for the Oxygen Reduction and the Oxygen Evolution Reactions

Inês S. Marques ¹, Bruno Jarrais ¹, Israël-Martyr Mbomekallé ², Anne-Lucie Teillout ², Pedro de Oliveira ², Cristina Freire ¹ and Diana M. Fernandes ^{1,*}

¹ REQUIMTE, Departamento de Química e Bioquímica, Faculdade de Ciências, Universidade do Porto, 4169-007 Porto, Portugal; up201608306@edu.fc.up.pt (I.S.M.); bjarrais@gmail.com (B.J.); acfreire@fc.up.pt (C.F.)

² Institut de Chimie Physique, UMR 8000 CNRS, Université Paris-Saclay, CEDEX, 91405 Orsay, France; israel.mbomekalle@universite-paris-saclay.fr (I.-M.M.); anne-lucie.teillout@universite-paris-saclay.fr (A.-L.T.); pedro.deoliveira@universite-paris-saclay.fr (P.d.O.)

* Correspondence: diana.fernandes@fc.up.pt

Abstract: The smart choice of polyoxometalates (POMs) and the design of POM@carbon-based composites are promising tools for producing active electrocatalysts for both the oxygen reduction (ORR) and the oxygen evolution reactions (OER). Hence, herein, we report the preparation, characterization and application of three composites based on doped, multi-walled carbon nanotubes (MWCNT_N6) and three different POMs ($\text{Na}_{12}[(\text{FeOH}_2)_2\text{Fe}_2(\text{As}_2\text{W}_{15}\text{O}_{56})_2]\cdot 54\text{H}_2\text{O}$, $\text{Na}_{12}[(\text{NiOH}_2)_2\text{Ni}_2(\text{As}_2\text{W}_{15}\text{O}_{56})_2]\cdot 54\text{H}_2\text{O}$ and $\text{Na}_{14}[(\text{FeOH}_2)_2\text{Ni}_2(\text{As}_2\text{W}_{15}\text{O}_{56})_2]\cdot 55\text{H}_2\text{O}$) as ORR and OER electrocatalysts in alkaline medium (pH = 13). Overall, the three POM@MWCNT_N6 composites showed good ORR performance with onset potentials between 0.80 and 0.81 V vs. RHE and diffusion-limiting current densities ranging from -3.19 to -3.66 mA cm⁻². Fe_4 @MWCNT_N6 and Fe_2Ni_2 @MWCNT_N6 also showed good stability after 12 h (84% and 80% of initial current). The number of electrons transferred per O₂ molecule was close to three, suggesting a mixed regime. Moreover, the Fe_2Ni_2 @MWCNT_N6 presented remarkable OER performance with an overpotential of 0.36 V vs. RHE (for $j = 10$ mA cm⁻²), a j_{max} close to 135 mA cm⁻² and fast kinetics with a Tafel slope of 45 mV dec⁻¹. More importantly, this electrocatalyst outperformed not only most POM@carbon-based composites reported so far but also the state-of-the-art RuO₂ electrocatalyst. Thus, this work represents a step forward towards bifunctional electrocatalysts using less expensive materials.

Keywords: polyoxometalates; oxygen reduction reaction; oxygen evolution reaction; carbon nanotubes; heteroatom doping



Citation: Marques, I.S.; Jarrais, B.; Mbomekallé, I.-M.; Teillout, A.-L.; de Oliveira, P.; Freire, C.; Fernandes, D.M. Synergetic Effects of Mixed-Metal Polyoxometalates@Carbon-Based Composites as Electrocatalysts for the Oxygen Reduction and the Oxygen Evolution Reactions. *Catalysts* **2022**, *12*, 440. <https://doi.org/10.3390/catal12040440>

Academic Editor: Maria Victoria Martínez Huerta

Received: 21 March 2022

Accepted: 12 April 2022

Published: 14 April 2022

Publisher's Note: MDPI stays neutral with regard to jurisdictional claims in published maps and institutional affiliations.



Copyright: © 2022 by the authors. Licensee MDPI, Basel, Switzerland. This article is an open access article distributed under the terms and conditions of the Creative Commons Attribution (CC BY) license (<https://creativecommons.org/licenses/by/4.0/>).

1. Introduction

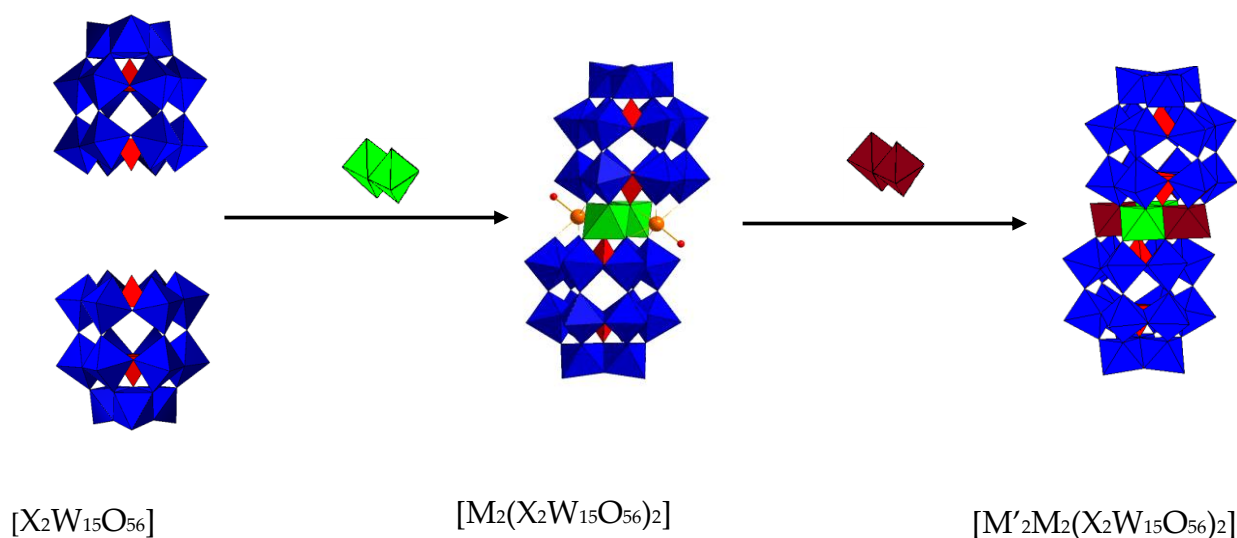
The current environmental and energy crisis has stimulated the demand for viable, sustainable and clean energy solutions for energy storage and conservation. The development of energy storage and conservation devices, such as fuel cells and water-splitting devices, aims to reduce the effects of energy demand [1,2]. The electrochemical processes that occur in these devices are the oxygen reduction reaction (ORR) at the cathode of the fuel cell and the oxygen evolution reaction (OER) at the anode of an electrolytic cell [3,4]. The fuel cell generates energy from O₂ and H₂, yielding water as a clean by-product, and the electrolytic cell uses electricity to split water into H₂ (fuel) and O₂ [5,6].

For the ORR, the most active electrocatalysts (ECs) so far are based on noble metals, such as Pt, and, for the OER, the most effective ECs are IrO₂ and RuO₂. However, these materials have some disadvantages, such as high cost, low abundance and intolerance to fuel crossover (methanol and CO). Besides, these materials do not work in both reactions; for

example, platinum-based materials have poor electrocatalytic activity for the OER because Pt oxidizes easily at large overpotentials [7–9]. So, these limitations and disadvantages have encouraged the growing search for new, more stable and economically viable alternatives. Therefore, possible alternatives to current electrocatalysts include carbon materials (CMs), polyoxometalates (POMs) and their corresponding hybrid materials POMs@CMs.

There are many types of carbon materials, including graphene and carbon nanotubes. These materials have advantages such as a high specific surface area, a symmetrical pore size and structure and a high electric conductivity [10,11], but their electrocatalytic activity may still be improved by doping with different heteroatoms such as nitrogen. The incorporation of nitrogen into the sp^2 carbon allows the tuning of the electronic properties of pristine carbon materials, giving rise to increased electrochemical performances and catalytic activities [12–14], improved tolerance to fuel crossover and higher versatility for a wide range of reactions [9]. The advantage of having electrocatalysts with high surface area and mesoporosity is that they can facilitate the adsorption of oxygen and, therefore, accelerate the surface reaction [15]. So, these advantages make carbon materials promising candidates for the ORR [12,16–22] and the OER [23–28].

Polyoxometalates, due to their high versatility, have potential applications in diverse areas ranging from catalysis, electroanalytical chemistry and materials science [29]. POMs are metal-oxo anionic clusters, the chemical properties of which can be controlled by transition metal substitution and the counter cation used [30]. They are ideal candidates for electrocatalysis because of their chemical properties, which can be adjusted as required by choosing the appropriate elements [31]. Undoubtedly, one of their most important properties is their ability to undergo reversible multivalent reductions/oxidations, leading to the formation of mixed valence species, which enable them with favorable electrocatalytic properties in relation to other electrochemical processes [32,33]. In recent years, the use of composites based on POMs and carbon nanomaterials as potential ECs for the ORR [34–36] and the OER [37–41] has been explored. The POMs used in this work are from the sandwich-type Dawson family and result from the reaction of a lacunary species $[X_2W_{15}O_{56}]^{12-}$ (where X = As, P, Si, Ge, B, Al, or Ga), with M (a d- or f-transition metal) to give the compound $[M_4(H_2O)_2(X_2W_{15}O_{56})_2]^{y-}$, in which the metal cluster $M_4O_{14}(H_2O)_2$ is sandwiched between two lacunary fragments (Scheme 1).



Scheme 1. Two-step formation of mixed, sandwich-type Dawson family derivatives, $[(M_2M'_2)(X_2W_{15}O_{56})_2]^{n-}$.

In these studies, we synthesized new composite materials based on multi-walled carbon nanotubes doped with nitrogen (MWCNT_N6) and Wells–Dawson sandwich polyoxometalates with M = Fe, Ni and both metals (Fe_2Ni_2) in order to understand the in-

fluence of the metal on the electrochemical performances towards both the ORR and the OER processes.

2. Experimental Section

2.1. Materials and Methods

Sodium acetate (99.5%, Merck, Algés, Portugal), acetic acid (100%, Merck, Algés, Portugal) and potassium hydroxide (99.99%, Sigma-Aldrich, Algés, Portugal) were used as received. Multi-walled carbon nanotubes (sample denoted as MWCNT) were commercially obtained from Nanocyl S.A., ref. 3100 MWCNT (>95% carbon purity; 9.5 nm average diameter, Sambreville, Belgium). Pt/C 20 wt% (HiSPEC[®] 3000, Alfa Aesar, Kandel, Germany), Nafion 117[®] (5 wt% in lower aliphatic alcohols and water, Aldrich, Algés, Portugal), isopropanol (99.5%, Aldrich, Algés, Portugal) and methanol (anhydrous, VWR, Amadora, Portugal) were also used directly. Ultra-pure water (18.2 MΩ cm at 25 °C, Interlab, Lisboa, Portugal) was used to prepare the solutions for materials synthesis and the electrolyte for the ORR and the OER tests. The materials prepared were characterized prior to their application through XPS and SEM/EDX, and the apparatus and the detailed methods used are described in the Supplementary Materials file.

Regarding the electrocatalytic tests, a PGSTAT 302N potentiostat (Autolab, Utrecht, The Netherlands) controlled by NOVA 2.1 was used. All details concerning the electrodes and the electrode preparation and modification are depicted in the file.

2.2. Materials Preparation

The tungstoarsenates $\text{Na}_{12}[(\text{FeOH}_2)_2\text{Fe}_2(\text{As}_2\text{W}_{15}\text{O}_{56})_2]\cdot 54\text{H}_2\text{O}$ (Fe_4), $\text{Na}_{12}[(\text{NiOH}_2)_2\text{Ni}_2(\text{As}_2\text{W}_{15}\text{O}_{56})_2]\cdot 54\text{H}_2\text{O}$ (Ni_4) and $\text{Na}_{14}[(\text{FeOH}_2)_2\text{Ni}_2(\text{As}_2\text{W}_{15}\text{O}_{56})_2]\cdot 55\text{H}_2\text{O}$ (Fe_2Ni_2) were prepared according to already described procedures [42–44].

The incorporation of nitrogen onto the pristine MWCNT was accomplished through mechanical treatment in ball-milling Retsch MM200 equipment using melamine as the precursor, followed by adequate thermal treatment under N_2 flow. Briefly, 0.60 g of MWCNT was mixed with 0.26 g of nitrogen using the melamine precursor, and the mixture was ball-milled for 5 h at a constant frequency of 15 vibrations s^{-1} . Then, the resulting material was subjected to a thermal treatment under N_2 flow (100 $\text{cm}^3 \text{min}^{-1}$) at a rate of 10 °C min^{-1} until it reached 600 °C, kept at that temperature for 1 h, cooled to room temperature under nitrogen atmosphere and stored in a desiccator.

The POM@MWCNT_N6 composites were then prepared through the immobilization of the three POMs onto the previously prepared MWCNT_N6. The immobilization of the POMs was achieved as follows: a 5 mL acetate buffer solution (pH = 4.0) containing 50 mg of POM was added to a 20 mL acetate buffer solution (pH = 4.0) containing 50 mg of MWCNT_N6. The mixture was dispersed for 15 min in an ultrasonic bath and then left to stir for 2 h at 400 rpm. Afterwards, the resulting composites were filtered, washed and left to dry at 60 °C under vacuum overnight. The composites were labelled as $\text{Fe}_4\text{@MWCNT_N6}$, $\text{Ni}_4\text{@MWCNT_N6}$ and $\text{Fe}_2\text{Ni}_2\text{@MWCNT_N6}$.

3. Results and Discussion

3.1. Electrocatalysts Characterization

3.1.1. X-ray Photoelectron Spectroscopy

All materials were analyzed by XPS to study their composition. The surface atomic percentages of each element for all the materials are presented in Table 1.

Table 1. XPS relative surface atomic percentages for all the materials ^a.

Sample	Atomic %							
	C1s	O1s	N1s	Na1s	Fe2p	Ni2p	As3p	W4f
MWCNT	98.84	1.16	-	-	-	-	-	-
MWCNT_N6	94.39	3.70	1.91	-	-	-	-	-
Fe ₄ @MWCNT_N6	90.62	6.76	1.21	0.76	0.05	-	0.05	0.55
Ni ₄ @MWCNT_N6	90.29	6.77	1.57	0.66	-	0.06	0.07	0.57
Fe ₂ Ni ₂ @MWCNT_N6	92.88	5.00	1.31	0.41	0.03	0.02	0.03	0.32

^a Determined by the areas of the respective bands in the high-resolution XPS spectra.

As can be seen in Table 1, the presence of nitrogen in the doped material (MWCNT_N6) was confirmed, indicating that the doping procedure was successful, and the composite materials atomic percentages also revealed that the POM was present. There was a significant oxygen percentage increase after the POM immobilization, asserting the POM presence in the composite materials. After the POM immobilization, there was also a decrease of the N1s' atomic percentage in the composite materials. Considering that XPS is a surface technique that analyzes depths up to 10 nm, the presence of the POM at the surface of the materials may have hindered the nitrogen detection. The N1s high-resolution XPS spectra of the N-containing prepared materials are shown in Figure 1, and the relative atomic percentages of nitrogen obtained in different chemical environments are presented in Table 2. The high-resolution XPS N1s spectra of the N-containing prepared materials were deconvoluted into three main peaks and assigned to pyridinic N (≈ 398.9 eV), pyrrolic N (≈ 400.6 eV) and quaternary N (≈ 402.8 eV) [45–47]. For the MWCNT_N6, a fourth peak at 405.5 eV was found and attributed to nitrogen oxide and/or nitrate species [45].

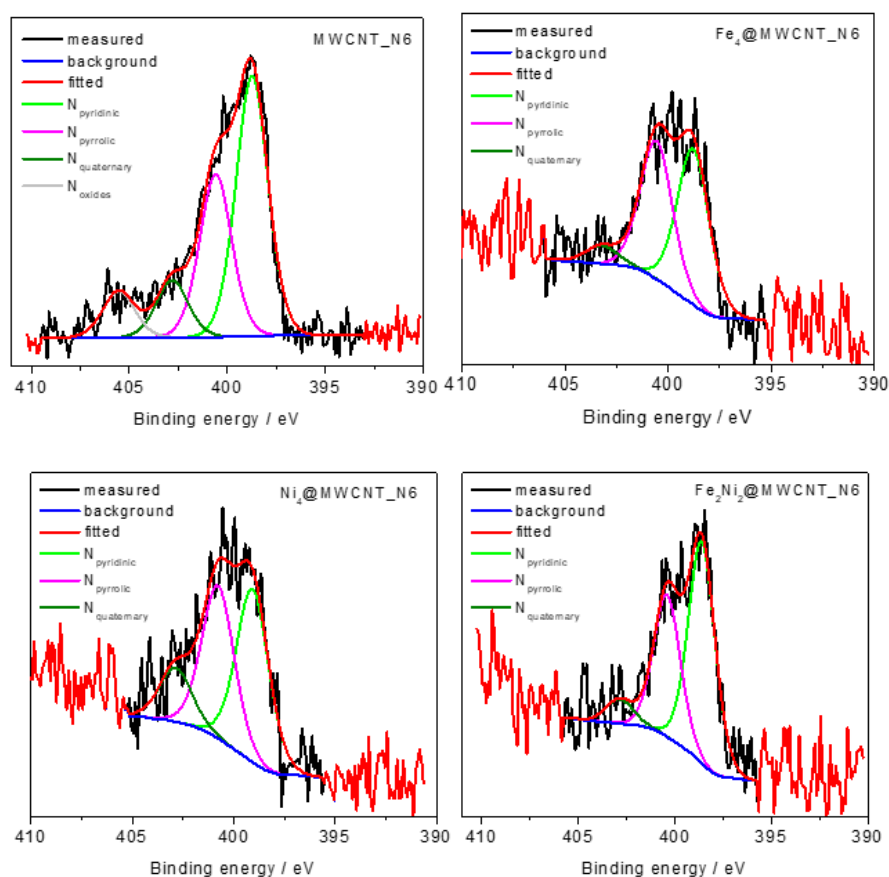


Figure 1. Deconvoluted N1s high-resolution spectra of MWCNT_N6-based materials (green: pyridinic N; pink: pyrrolic N; olive: quaternary N; gray: N-oxides/nitrates).

Table 2. Relative atomic percentages of nitrogen obtained from the XPS high-resolution N1s spectra of the prepared carbon materials.

Material	% N			
	≈398.9 eV (Pyridinic N)	≈400.6 eV (Pyrrolic N)	≈402.8 eV (Quaternary N)	≈405.5 eV (N-Oxides)
MWCNT_N6	49.3	30.9	10.9	8.9
Fe ₄ @MWCNT_N6	49.8	44.3	5.9	-
Ni ₄ @MWCNT_N6	45.6	40.2	14.2	-
Fe ₂ Ni ₂ @MWCNT_N6	57.0	36.6	6.4	-

The C1s high-resolution spectra of all the materials are shown in Figure S1 and were deconvoluted as follows: a main peak at 284.6 eV was assigned to sp² C, characteristic of graphitic structures; a peak at 285.2 eV corresponded to the sp³ C hybridization; a peak at 285.9 eV was attributed to C–N; a peak at 286.9 eV was ascribed to C in C–O–C; a peak at 288.2 eV was assigned to C in C=O; a peak at 289.3 eV corresponded to C in O–C=O; and a peak at 290.7 eV was attributed to π–π* transitions [48]. For the MWCNT_N6, the deconvolution of the O1s high-resolution XPS spectrum (Figure S2) was not possible, but, still, the peak at 532.7 eV had the contribution of O in the C=O, COOH and C–OH groups. On the other hand, in the O1s spectra of all POM-containing materials (Figure S2), it was possible to identify a peak at 531.1 eV, associated with O in the C=O and COOH groups, and a second peak at 533.0 eV, attributed to O in the C–OH groups [49,50]. The peak at lower binding energies also had the contribution of O in O–W arising from the presence of the polyoxometalate. The Fe2p high-resolution spectra of Fe₄@MWCNT_N6 and Fe₂Ni₂@MWCNT_N6 showed a peak at 710.8 eV corresponding to 2p^{3/2} (Figures S3 and S5). The corresponding 2p^{1/2} was difficult to attribute due to the low signal-to-noise ratio. The same difficulty was encountered in the deconvolution of the Ni2p spectra. Both Ni₄@MWCNT_N6 and Fe₂Ni₂@MWCNT_N6 showed a peak at ≈856.5 eV, assigned to 2p^{3/2} (Figures S4 and S5). All POM-containing materials also showed the presence of arsenic and tungsten, but, since As3d and W4f appeared in the same region, the percentage of arsenic was estimated from the As3p high-resolution spectra, which presented one peak at ≈145 eV. In the W4f high-resolution spectra, the peaks could be resolved as 4f^{7/2} and 4f^{5/2} doublets that appeared at ≈ 36.0 eV and ≈ 38.2 eV, respectively [3]. The signal of Na1s for the three POM-containing materials was due to the presence of the POM counter cations in the final compounds.

3.1.2. Scanning Electron Microscopy

The morphology of the three composites prepared was assessed by SEM. Figure 2 shows the SEM images for Fe₂Ni₂@MWCNT_N6 at two magnifications, while the corresponding images for Fe₄@MWCNT_N6 and Ni₄@MWCNT_N6 are depicted in Figure S6. The SEM images at lower magnification (×5000) show a roughened texture, while, under higher magnification (×50,000), it is possible to observe the carbon nanotubes. An EDX elemental mapping analysis (Figure 3, Figures S7 and S8) was further conducted to assess the presence and distribution of the POMs in the composites. The EDX spectra showed the presence of C and O from the carbon materials and As, W and O from the POMs. The presence of Fe was also observed for Fe₄@MWCNT_N6 (Figure S7) and Fe₂Ni₂@MWCNT_N6, and the presence of Ni was observed for Ni₄@MWCNT_N6 (Figure S8) and Fe₂Ni₂@MWCNT_N6. The elemental mapping analysis also revealed a homogeneous distribution of all the elements throughout the composites, suggesting a uniform immobilization of the polyoxometalates throughout the MWCNT_N6.

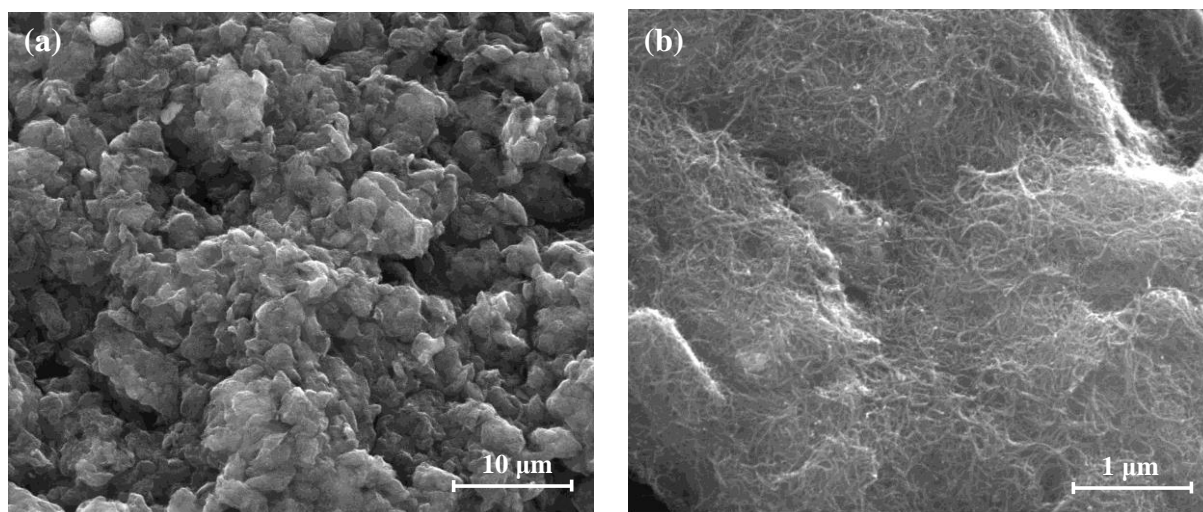


Figure 2. SEM images of Fe₂Ni₂@MWCNT_N6 at ×5000 (a) and ×50,000 (b) magnification.

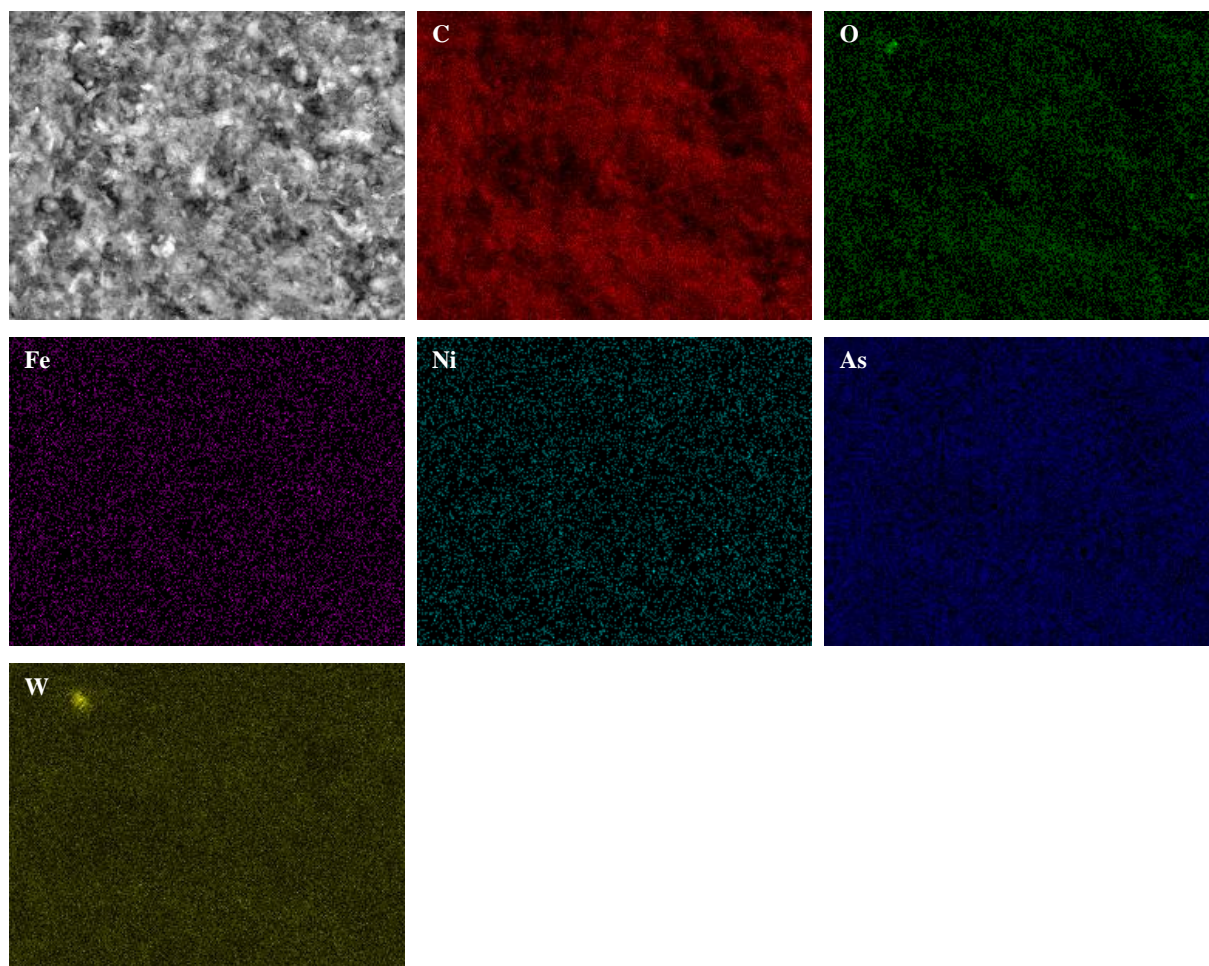


Figure 3. SEM and EDX elemental mapping images of Fe₂Ni₂@MWCNT_N6 at ×2500 magnification.

3.2. Electrochemical Performance of the Electrocatalysts towards the ORR

Initially, the ORR electrocatalytic performances of Fe₄@MWCNT_N6, Ni₄@MWCNT_N6 and Fe₂Ni₂@MWCNT_N6 were assessed by cyclic voltammetry (CV) in KOH saturated with nitrogen and with oxygen. The CVs of the three prepared composites are depicted in Figure S9, where it can be clearly observed that, when oxygen is absent no peak can be

detected, whereas, in O_2 -saturated electrolyte, all composites present an irreversible reduction peak corresponding to the reduction of oxygen at $E_{pc} = 0.74, 0.75$ and 0.75 V vs. RHE for $Fe_4@MWCNT_N6$, $Ni_4@MWCNT_N6$ and $Fe_2Ni_2@MWCNT_N6$, respectively. Pt/C and MWCNT_N6 were also evaluated in the same experimental conditions, presenting the ORR peak at $E_{pc} = 0.86$ and 0.76 V vs. RHE, respectively.

Further evaluation of the ORR electrocatalytic performances of the prepared composites was conducted by linear sweep voltammetry (LSV) in the same electrolyte saturated in both N_2 and O_2 . The LSVs at 1600 rpm of MWCNT_N6, $Fe_4@MWCNT_N6$, $Ni_4@MWCNT_N6$, $Fe_2Ni_2@MWCNT_N6$ and Pt/C are shown in Figure 4a, and the key ORR parameters are depicted in Table 3. It is important to note that these LSVs correspond to those in O_2 -saturated KOH after subtraction of the blanks (corresponding LSVs in N_2 -saturated KOH). As can be observed, $Fe_4@MWCNT_N6$ and $Ni_4@MWCNT_N6$ presented practically identical diffusion-limiting current density values ($j_L = -3.19$ and -3.20 $mA\ cm^{-2}$, respectively) while, for $Fe_2Ni_2@MWCNT_N6$, the value increased to $j_L = -3.66$ $mA\ cm^{-2}$. These values are somewhat far from that obtained for Pt/C (-4.68 $mA\ cm^{-2}$); still, it is clear that the introduction of POMs produced an improvement in the j_L values leading to an increase of $\approx 20\%$ for $Fe_4@MWCNT_N6$ and $Ni_4@MWCNT_N6$ and 37% for $Fe_2Ni_2@MWCNT_N6$ when compared with the MWCNT_N6.

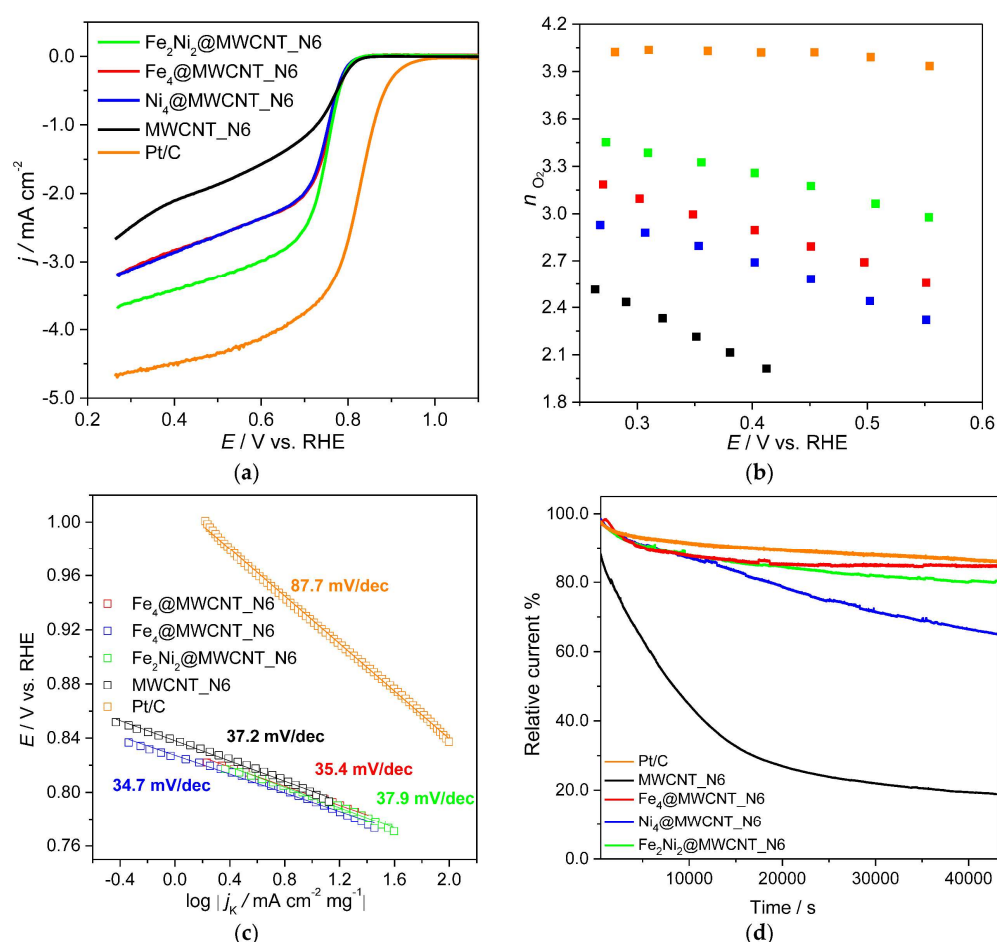


Figure 4. ORR LSV curves obtained in KOH (0.1 M) saturated with O_2 for MWCNT_N6, $Fe_4@MWCNT_N6$, $Ni_4@MWCNT_N6$, $Fe_2Ni_2@MWCNT_N6$ and Pt/C at 1600 rpm and $0.005\ V\ s^{-1}$ (a), n_{O_2} at several potential values (b), ORR Tafel plots (c) and chronoamperometric responses in KOH (0.1 M) saturated with O_2 at 1600 rpm for 43,200 s (d).

Table 3. The ORR performance parameters for all the materials tested.

Sample	E_{onset} (5% Total)	E_{onset} ($j = 0.1 \text{ mA cm}^{-2}$)	j_{L} (mA cm^{-2})	Tafel (mV dec^{-1})	n_{O_2}
Pt/C	0.91	0.94	−4.68	87.7	4.0
MWCNT_N6	0.81	0.81	−2.67	37.2	2.3
Fe ₄ @MWCNT_N6	0.80	0.81	−3.19	35.4	2.9
Ni ₄ @MWCNT_N6	0.80	0.80	−3.20	34.7	2.7
Fe ₂ Ni ₂ @MWCNT_N6	0.81	0.80	−3.66	37.9	3.2

Even though the E_{onset} can be determined by different methods [31,51,52], we assumed the potential corresponded to 5% of the diffusion-limiting current density. The values for all materials were similar (0.80–0.81 V vs. RHE), while, for Pt/C, a value of 0.91 V vs. RHE was obtained.

The number of electrons transferred per O₂ molecule (n_{O_2}) was estimated by applying the Koutecky–Levich equation to the LSVs (Figure S10) acquired at different rotation speeds (400 to 3000 rpm). Figure 4b shows the n_{O_2} values vs. the applied potential, and Figure S11 shows the K–L plots. As can be observed, the values of j^{-1} increased with increasing $\omega^{-1/2}$, suggesting a first-order electrocatalytic O₂ reduction with respect to the concentration of dissolved oxygen. Moreover, the K–L plots of the three POM@MWCNT_N6 composites prepared presented different slopes, indicating a dependency of n_{O_2} on the applied potential. The mean n_{O_2} value obtained for Fe₄@MWCNT_N6, Ni₄@MWCNT_N6 and Fe₂Ni₂@MWCNT_N6 was 2.9, 2.7 and 3.2, respectively, while, for Pt/C, a value of 4.0 was obtained. The ORR process, in alkaline medium, can proceed through either an indirect (2-electrons) pathway or a direct (4-electrons) one. The first involves the reduction of O₂ to HO₂[−] and then the intermediate's reduction to H₂O/HO[−], while, in the second, O₂ is directly reduced to H₂O/HO[−] [31]. Therefore, the results obtained for the three POM@MWCNT_N6 composites suggest a mixed regime. Similar behavior was already reported for other POM@carbon-based materials [3]. On the other hand, Pt/C was involved in a direct process with $n_{\text{O}_2} = 4.0$.

The Tafel plots (Figure 4c) were obtained from the LSV data in Figure 4a in 0.1 M KOH saturated with O₂ at 1600 rpm. The Tafel slopes obtained between $E = 1.00$ and 0.76 V vs. RHE were 37.2, 35.3, 34.7, 37.9 and 87.7 mV dec^{−1} for MWCNT_N6, Fe₄@MWCNT_N6, Ni₄@MWCNT_N6, Fe₂Ni₂@MWCNT_N6 and Pt/C, respectively. These values suggest that oxygen molecules were easily adsorbed and activated at the surface of these materials and that conversion of MOO[−] to MOOH ruled the overall reaction rate (M stands for an empty site on the electrocatalyst surface) [53].

To obtain more insights about the effect of the immobilization of different POMs on the intrinsic ORR activity, the current density values were normalized to the corresponding double-layer capacitances (Figure S12) considered as an approximation of the electrochemically active surface areas (ECSAs). By applying this correction, it was possible to discard the influence of surface areas both from the support (MWCNT_N6) and the final composite (POM@MWCNT_N6). The similar nature of the materials evaluated in this work and the proportional relationship between the ECSA and the double-layer capacitance (C_{dl}) made it possible to compare the materials' C_{dl} values. The double-layer capacitance values were determined via charging tests consisting of CV measurements at increasing scan rates (see full details in SI file and Figures S13 and S14). So, C_{dl} values were calculated from the slopes of the linear fittings of CV current densities (measured at the same potential of 1.15 V vs. RHE, $j_{1.15}$) reached at different scan rates (Figure S15). Still, these calculated capacitance values must be seen as estimated values due to the existence of some faradaic contributions in the CV plots of the charge–discharge tests. In this context, the C_{dl} can be considered as an estimation of the number of accessible electrocatalytically active sites for a particular electrocatalyst [54]. The C_{dl} values obtained were 1.4, 9.0, 9.3, 2.6 and 6.3 $\mu\text{F cm}^{-2}$ for MWCNT_N6, Fe₄@MWCNT_N6, Ni₄@MWCNT_N6, Fe₂Ni₂@MWCNT_N6 and Pt/C, respectively. As can be observed in Figure S12, the electroactive surface area had a significant

impact on the ORR performance. These studies suggest that the immobilization of Fe₄ and Ni₄ onto the MWCNT_N6 may not be advantageous as both these composite materials presented the lowest performance. Oppositely, the Fe₂Ni₂@MWCNT_N6 performed better than the MWCNT_N6 alone and even better than Pt/C in terms of the j_L values. Additionally, there was a clear synergetic effect in the Fe₂Ni₂@MWCNT_N6 as this composite had a huge increase of the ORR activity when compared with the materials containing POMs with only one type of transition metal (Fe₄@MWCNT_N6 and Ni₄@MWCNT_N6). This suggests that the presence of mixed transition metals may be the solution to improve performance.

The stability of MWCNT_N6, Fe₄@MWCNT_N6, Ni₄@MWCNT_N6, Fe₂Ni₂@MWCNT_N6 and Pt/C was also evaluated, as this is an important parameter when evaluating the performance of an electrocatalyst. This was assessed by chronoamperometry at $E = 0.50$ V vs. RHE for 12 h in oxygen-saturated alkaline electrolyte, and the results are depicted in Figure 4d. The Pt/C electrocatalyst showed a good stability by retaining 86% of its initial current density after 12 h. The Fe₄@MWCNT_N6 composite presented the best retaining percentage of 84%, followed by Fe₂Ni₂@MWCNT_N6 (80%), Ni₄@MWCNT_N6 (65%) and MWCNT_N6 (19%).

3.3. Electrochemical Performance of the Electrocatalysts towards the OER

The prepared electrocatalysts were also evaluated towards the OER in alkaline media, and the LSVs are depicted in Figure 5a, while the most important parameters are presented in Table 4. One of the parameters that is commonly determined to evaluate the OER electrocatalyst's performance is the potential that is needed to reach $j = 10$ mA cm⁻², a value corresponding to the current density anticipated at the electrode in a solar water-splitting device (under sunlight) with an efficiency of 10% [31]. Thus, generally, the overpotential (η_{10}) at $j = 10$ mA cm⁻² is taken as a reference point. As observed, the three POM@MWCNT_N6 composites presented relatively low η_{10} values of 0.58, 0.46 and 0.36 V for Fe₄@MWCNT_N6, Ni₄@MWCNT_N6 and Fe₂Ni₂@MWCNT_N6, respectively. This last composite also presented the highest current density at $E_p = 1.86$ V vs. RHE (134.6 mA cm⁻²), being much higher than the values obtained for Fe₄@MWCNT_N6 (13.7 mA cm⁻²) and Ni₄@MWCNT_N6 (30.9 mA cm⁻²). These results suggest that a possible synergetic effect occurs when the POM presents both metals (Fe and Ni). The incorporation of Fe possibly helps in activating the electrochemical processes of Ni (well-known active oxygen evolution center), leading to an enhanced electrocatalytic activity but, at the same time, improves the conductivity of the composite material.

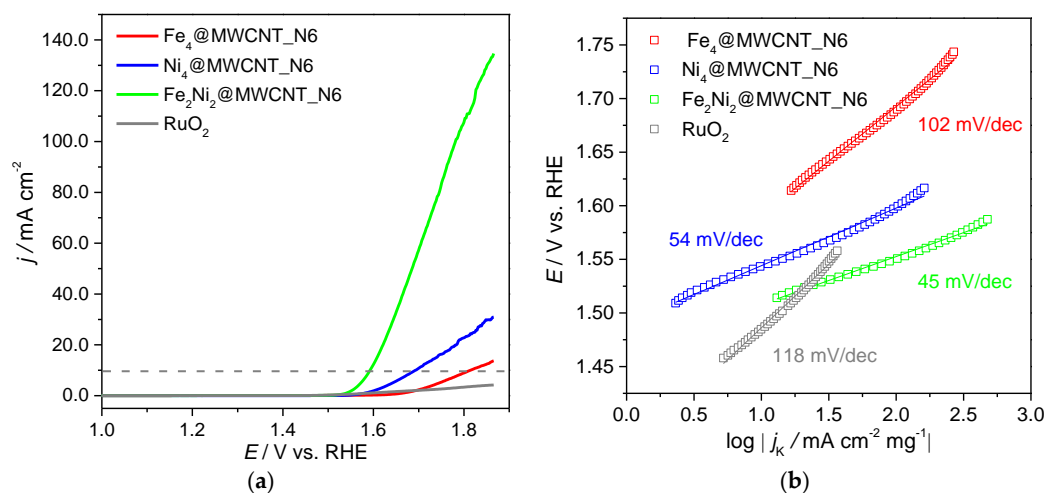


Figure 5. LSV OER curves (a) and Tafel plots (b) of Fe₄@MWCNT_N6, Ni₄@MWCNT_N6 and Fe₂Ni₂@MWCNT_N6.

Table 4. The OER performance parameters for all the materials tested.

Sample	E_{10}	η_{10} ($j = 0.1 \text{ mA cm}^{-2}$)	j_{max} (mA cm^{-2})	Tafel (mV dec^{-1})
RuO ₂	-	-	4.14	118
Fe ₄ @MWCNT_N6	1.81	0.58	13.7	102
Ni ₄ @MWCNT_N6	1.69	0.46	30.9	54
Fe ₂ Ni ₂ @MWCNT_N6	1.59	0.36	134.6	45

The Tafel slopes were determined using the LSVs from Figure 5a, and the Tafel plots are shown in Figure 5b. Fe₂Ni₂@MWCNT_N6 presented the lowest Tafel slope (45 mV dec⁻¹), followed by Ni₄@MWCNT_N6 (54 mV dec⁻¹) and Fe₄@MWCNT_N6 (102 mV dec⁻¹), suggesting faster kinetics for the first two composites. All these metrics are increasingly close to those collected in the bibliography (obtained under similar testing conditions) for the expensive, state-of-the-art references: RuO₂ with $\eta_{10} = 0.30$ V, Tafel slope = 65 mV dec⁻¹ and IrO₂ with $\eta_{10} = 0.36$ V and Tafel slope = 82 mV dec⁻¹ [55]. Still, we evaluated the performance of commercial RuO₂ under the same experimental conditions. However, our OER results were very far from those reported [56–58]. According to the literature, the preparation method has a huge influence on the OER performances of both IrO₂ and RuO₂ [57,58]. In addition, the electrocatalysts electroactive surface also has an influence on their electrocatalytic performances. Therefore, as for the ORR, the OER current densities were normalized to the corresponding double-layer capacitances (Figure S16). This correction highlights even more that Fe₂Ni₂@MWCNT_N6 was the best performing composite for the OER from all the materials tested, including the RuO₂. Our results with Ni₄@MWCNT_N6 and Fe₄@MWCNT_N6 are comparable with those reported in the literature (Table S1) for other POM-containing composites, but Fe₂Ni₂@MWCNT_N6 outperformed all, even the Co-containing POMs well known for their good OER activities [59–62]. Compared with other metal-oxide-containing composites, our results outperformed some [63–65], but others presented even lower overpotentials (0.28–0.32 V) [66–68].

The stability of the three electrocatalysts prepared was assessed by chronoamperometry, and the results are collected in Figure S17. All plots show the characteristic, local current density drops originated by oxygen bubble formation on the electrode surface. For the Ni₄@MWCNT_N6 composite, previous current density values were partially recovered with bubble release, and this electrocatalyst showed a good stability with a current retention of 87% after 12 h at a fixed potential of 0.50 V vs. RHE. For the Fe₄@MWCNT_N6, there was an initial increase in the current, but then it showed the typical behavior, presenting a current retention of 80%. Unfortunately, the Fe₂Ni₂@MWCNT_N6 composite presented the worst performance in terms of stability, with a current retention of 64% after the same 12 h.

4. Conclusions

Three POM@MWCNT_N6 composites based on [M₄(H₂O)₂(X₂W₁₅O₅₆)₂]^{y-} with M₄ = Fe₄, Ni₄ and Fe₂Ni₂ were successfully prepared by a simple and scalable strategy without the need for linker molecules. The prepared composites showed good, intrinsic electrocatalytic activity toward the ORR, but a mixed regime was observed instead of the envisaged selectivity for the 4-electron process. Still, the Fe₂Ni₂@MWCNT_N6 showed the best performance with a $n_{\text{O}_2} = 3.2$ and a diffusion-limiting current density of -3.66 mA cm^{-2} . Additionally, Fe₄@MWCNT_N6 and Fe₂Ni₂@MWCNT_N6 also showed good stability.

Most importantly, Fe₂Ni₂@MWCNT_N6 presented a remarkable OER performance, outperforming most of the reported results for other composites based on POMs and carbon materials and reaching an overpotential of 0.36 V vs. RHE (for $j = 10 \text{ mA cm}^{-2}$) and a current density of 135 mA cm^{-2} at $E_p = 1.86$ V vs. RHE. Moreover, in the same experimental conditions, it surpassed the state-of-the-art RuO₂ electrocatalyst. Surprisingly, the results were much better than those for the composites containing POMs with just one type of

transition metal in the equatorial plane, which suggests a possible synergetic effect between the two types of metal resulting in an improvement of the electrochemical performances.

Future studies with POMs containing other transition metals will be conducted to confirm these findings but also to unravel the overall reaction mechanisms.

Supplementary Materials: The following supporting information can be downloaded at: <https://www.mdpi.com/article/10.3390/catal12040440/s1>. Figure S1. Deconvoluted C1s high-resolution spectra of the MWCNT_N6-based materials; Figure S2. Deconvoluted O1s high-resolution spectra of the MWCNT_N6-based materials; Figure S3. Deconvoluted high-resolution spectra for Fe₄@MWCNT_N6: Na1s (a), Fe2p (b), As3p (c) and W4f (d); Figure S4. Deconvoluted high-resolution spectra for Ni₄@MWCNT_N6: Na1s (a), Ni2p (b), As3p (c) and W4f (d); Figure S5. Deconvoluted high-resolution spectra for Fe₂Ni₂@MWCNT_N6: Na1s (a), Fe2p (b), Ni2p (c), As3p (d) and W4f (e); Figure S6. SEM images of Fe₄@MWCNT_N6 and Ni₄@MWCNT_N6 at ×5000 (a,b) and ×50,000 (c,d) magnification; Figure S7. SEM and EDX elemental mapping images of Fe₄@MWCNT_N6 at ×2500 magnification; Figure S8. SEM and EDX elemental mapping images of Ni₄@MWCNT_N6 at ×2500 magnification; Figure S9. CVs of MWCNT_N6 (a), Fe₄@MWCNT_N6 (b), Ni₄@MWCNT_N6 (c), Fe₂Ni₂@MWCNT_N6 (d) and Pt/C (e) in N₂- (dash line) and O₂-saturated (red line) 0.1 M KOH at 5 mV s⁻¹; Figure S10. ORR LSVs of MWCNT_N6 (a), Fe₄@MWCNT_N6 (b), Ni₄@MWCNT_N6 (c), Fe₂Ni₂@MWCNT_N6 (d) and Pt/C (e) acquired at different rotation rates in O₂-saturated 0.1 M KOH solution at 5 mV s⁻¹; Figure S11. Koutecky–Levich (K-L) plots of MWCNT_N6 (a), Fe₄@MWCNT_N6 (b), Ni₄@MWCNT_N6 (c), Fe₂Ni₂@MWCNT_N6 (d) and Pt/C (e); Figure S12. ORR LSV curves obtained in KOH (0.1 M) saturated with O₂ at 1600 rpm and 0.005 V s⁻¹ with current densities normalized to the respective double-layer capacitance values; Figure S13. CVs at different scan rates for MWCNT_N6 (a), Fe₄@MWCNT_N6 (b), Ni₄@MWCNT_N6 (c) and Fe₂Ni₂@MWCNT_N6 (d) in N₂-saturated KOH (0.1 M); Figure S14. CVs at different scan rates of Pt/C and RuO₂ in N₂-saturated KOH (0.1 M); Figure S15. Current density scan rate linear fitting plots for all materials. Numeric values correspond to the double-layer capacitances (C_{dl}) for each material; Figure S16. OER LSV curves obtained in KOH (0.1 M) saturated with N₂ at 1600 rpm and 0.005 V s⁻¹ with current densities normalized to the respective double-layer capacitance values; Figure S17. Chronoamperometric responses in KOH (0.1 M) saturated with N₂ at 1600 rpm for 43,200 s; Table S1. Comparison of the OER electrochemical performance (overpotentials (η₁₀) and current density (j)) for POM-based composite materials reported in literature [6,41,54,63–77].

Author Contributions: The synthesis and characterization of POMs were performed by I.-M.M. and A.-L.T.; doped MWCNT by B.J.; and composite materials by I.S.M. The electrocatalytic experiments were conducted by D.M.F. and I.S.M. The research was supervised by D.M.F., P.d.O. and C.F.; and I.S.M. and D.M.F. were responsible for writing up the manuscript, which was proofread by D.M.F. and P.d.O. All authors have read and agreed to the published version of the manuscript.

Funding: This research was funded by Fundação para a Ciência e a Tecnologia through project PTDC/QUI-ELT/28299/2017 (FOAM4NER) and Programa Pessoa, and the APC was funded by the public Budget—OE by Fundação para a Ciência e a Tecnologia through the project UIDB/50006/2020 and UIDP/50006/2020.

Acknowledgments: Acknowledgments are also due to the FCT—project UID/QUI/50006/2013-POCI/01/0145/FEDER/007265, as well as to Campus France—project PHC Pessoa 42341RM (O₂@nanoCPOM). D.F. acknowledges the FCT/MCTES by the work contracts (in the scope of the framework contract foreseen in the numbers 4, 5 and 6 of article 23 of the Decree Law 57/2016 of 29 August, changed by Law 57/2017 of 19 July) supported by national funds (OE). I.-M.M., A.-L.T. and P.d.O. thank the CNRS and the Université Paris-Saclay for financial support.

Conflicts of Interest: The authors declare that they have no conflict of interest.

References

1. Seh, Z.W.; Kibsgaard, J.; Dickens, C.F.; Chorkendorff, I.B.; Norskov, J.K.; Jaramillo, T.F. Combining theory and experiment in electrocatalysis: Insights into materials design. *Science* **2017**, *355*, eaad4998. [[CrossRef](#)] [[PubMed](#)]
2. Kado, Y.; Soneda, Y.; Hatori, H.; Kodama, M. Advanced carbon electrode for electrochemical capacitors. *J. Solid State Electrochem.* **2019**, *23*, 1061–1081. [[CrossRef](#)]

3. Fernandes, D.M.; Novais, H.C.; Bacsá, R.; Serp, P.; Bachiller-Baeza, B.; Rodríguez-Ramos, I.; Guerrero-Ruiz, A.; Freire, C. Polyoxotungstate@Carbon Nanocomposites as Oxygen Reduction Reaction (ORR) Electrocatalysts. *Langmuir* **2018**, *34*, 6376–6387. [[CrossRef](#)] [[PubMed](#)]
4. Kuang, M.; Zheng, G.F. Nanostructured Bifunctional Redox Electrocatalysts. *Small* **2016**, *12*, 5656–5675. [[CrossRef](#)] [[PubMed](#)]
5. Katsounaros, I.; Cherevko, S.; Zeradjanin, A.R.; Mayrhofer, K.J.J. Oxygen Electrochemistry as a Cornerstone for Sustainable Energy Conversion. *Angew. Chem. Int. Ed.* **2014**, *53*, 102–121. [[CrossRef](#)]
6. Fernandes, D.M.; Mathumba, P.; Fernandes, A.J.S.; Iwuoha, E.I.; Freire, C. Towards efficient oxygen reduction reaction electrocatalysts through graphene doping. *Electrochim. Acta* **2019**, *319*, 72–81. [[CrossRef](#)]
7. Dun, R.M.; Hao, M.G.; Su, Y.M.; Li, W.M. Fe-N-doped hierarchical mesoporous carbon nanomaterials as efficient catalysts for oxygen reduction in both acidic and alkaline media. *J. Mater. Chem. A* **2019**, *7*, 12518–12525. [[CrossRef](#)]
8. Zhu, Y.L.; Zhou, W.; Yu, J.; Chen, Y.B.; Liu, M.L.; Shao, Z.P. Enhancing Electrocatalytic Activity of Perovskite Oxides by Tuning Cation Deficiency for Oxygen Reduction and Evolution Reactions. *Chem. Mater.* **2016**, *28*, 1691–1697. [[CrossRef](#)]
9. Gao, K.; Wang, B.; Tao, L.; Cuning, B.V.; Zhang, Z.P.; Wang, S.Y.; Ruoff, R.S.; Qu, L.T. Efficient Metal-Free Electrocatalysts from N-Doped Carbon Nanomaterials: Mono-Doping and Co-Doping. *Adv. Mater.* **2019**, *31*, 1805121. [[CrossRef](#)]
10. Frackowiak, E.; Beguin, F. Carbon materials for the electrochemical storage of energy in capacitors. *Carbon* **2001**, *39*, 937–950. [[CrossRef](#)]
11. Wang, Y.G.; Song, Y.F.; Xia, Y.Y. Electrochemical capacitors: Mechanism, materials, systems, characterization and applications. *Chem. Soc. Rev.* **2016**, *45*, 5925–5950. [[CrossRef](#)] [[PubMed](#)]
12. Zhu, Y.P.; Guo, C.X.; Zheng, Y.; Qiao, S.Z. Surface and Interface Engineering of Noble-Metal-Free Electrocatalysts for Efficient Energy Conversion Processes. *Acc. Chem. Res.* **2017**, *50*, 915–923. [[CrossRef](#)] [[PubMed](#)]
13. Ma, R.G.; Lin, G.X.; Zhou, Y.; Liu, Q.; Zhang, T.; Shan, G.C.; Yang, M.H.; Wang, J.C. A review of oxygen reduction mechanisms for metal-free carbon-based electrocatalysts. *NPJ Comput. Mater.* **2019**, *5*, 78. [[CrossRef](#)]
14. Tang, C.; Zhang, Q.; Zhao, M.Q.; Huang, J.Q.; Cheng, X.B.; Tian, G.L.; Peng, H.J.; Wei, F. Nitrogen-doped aligned carbon nanotube/graphene sandwiches: Facile catalytic growth on bifunctional natural catalysts and their applications as scaffolds for high-rate lithium-sulfur batteries. *Adv. Mater.* **2014**, *26*, 6100–6105. [[CrossRef](#)]
15. Pham, D.T.; Li, B.; Lee, Y.H. Nitrogen-doped activated graphene/SWCNT hybrid for oxygen reduction reaction. *Curr. Appl. Phys.* **2016**, *16*, 1242–1249. [[CrossRef](#)]
16. Guo, D.H.; Shibuya, R.; Akiba, C.; Saji, S.; Kondo, T.; Nakamura, J. Active sites of nitrogen-doped carbon materials for oxygen reduction reaction clarified using model catalysts. *Science* **2016**, *351*, 361–365. [[CrossRef](#)]
17. Sheng, Z.H.; Shao, L.; Chen, J.J.; Bao, W.J.; Wang, F.B.; Xia, X.H. Catalyst-Free Synthesis of Nitrogen-Doped Graphene via Thermal Annealing Graphite Oxide with Melamine and Its Excellent Electrocatalysis. *ACS Nano* **2011**, *5*, 4350–4358. [[CrossRef](#)]
18. Silva, R.; Voiry, D.; Chhowalla, M.; Asefa, T. Efficient Metal-Free Electrocatalysts for Oxygen Reduction: Polyaniline-Derived N- and O-Doped Mesoporous Carbons. *J. Am. Chem. Soc.* **2013**, *135*, 7823–7826. [[CrossRef](#)]
19. Chen, S.; Bi, J.Y.; Zhao, Y.; Yang, L.J.; Zhang, C.; Ma, Y.W.; Wu, Q.; Wang, X.Z.; Hu, Z. Nitrogen-Doped Carbon Nanocages as Efficient Metal-Free Electrocatalysts for Oxygen Reduction Reaction. *Adv. Mater.* **2012**, *24*, 5593–5597. [[CrossRef](#)]
20. Qu, L.T.; Liu, Y.; Baek, J.B.; Dai, L.M. Nitrogen-Doped Graphene as Efficient Metal-Free Electrocatalyst for Oxygen Reduction in Fuel Cells. *ACS Nano* **2010**, *4*, 1321–1326. [[CrossRef](#)]
21. Matter, P.H.; Zhang, L.; Ozkan, U.S. The role of nanostructure in nitrogen-containing carbon catalysts for the oxygen reduction reaction. *J. Catal.* **2006**, *239*, 83–96. [[CrossRef](#)]
22. Hu, C.G.; Dai, L.M. Carbon-Based Metal-Free Catalysts for Electrocatalysis beyond the ORR. *Angew. Chem. Int. Ed.* **2016**, *55*, 11736–11758. [[CrossRef](#)] [[PubMed](#)]
23. Zhang, J.T.; Zhao, Z.H.; Xia, Z.H.; Dai, L.M. A metal-free bifunctional electrocatalyst for oxygen reduction and oxygen evolution reactions. *Nat. Nanotechnol.* **2015**, *10*, 444–452. [[CrossRef](#)] [[PubMed](#)]
24. Wu, G.; Zelenay, P. Nanostructured Nonprecious Metal Catalysts for Oxygen Reduction Reaction. *Acc. Chem. Res.* **2013**, *46*, 1878–1889. [[CrossRef](#)]
25. Tian, G.L.; Zhao, M.Q.; Yu, D.S.; Kong, X.Y.; Huang, J.Q.; Zhang, Q.; Wei, F. Nitrogen-Doped Graphene/Carbon Nanotube Hybrids: In Situ Formation on Bifunctional Catalysts and Their Superior Electrocatalytic Activity for Oxygen Evolution/Reduction Reaction. *Small* **2014**, *10*, 2251–2259. [[CrossRef](#)]
26. Liu, Z.J.; Zhao, Z.H.; Wang, Y.Y.; Dou, S.; Yan, D.F.; Liu, D.D.; Xia, Z.H.; Wang, S.Y. In Situ Exfoliated, Edge-Rich, Oxygen-Functionalized Graphene from Carbon Fibers for Oxygen Electrocatalysis. *Adv. Mater.* **2017**, *29*, 1606207. [[CrossRef](#)]
27. Lyu, F.L.; Wang, Q.F.; Choi, S.M.; Yin, Y.D. Noble-Metal-Free Electrocatalysts for Oxygen Evolution. *Small* **2019**, *15*, 1804201. [[CrossRef](#)]
28. Qian, Y.H.; Hu, Z.G.; Ge, X.M.; Yang, S.L.; Peng, Y.W.; Kang, Z.X.; Liu, Z.L.; Lee, J.Y.; Zhao, D. A metal-free ORR/OER bifunctional electrocatalyst derived from metal-organic frameworks for rechargeable Zn-Air batteries. *Carbon* **2017**, *111*, 641–650. [[CrossRef](#)]
29. Katsoulis, D.E. A survey of applications of polyoxometalates. *Chem. Rev.* **1998**, *98*, 359–387. [[CrossRef](#)]
30. Li, G.; Ding, Y.; Wang, J.; Wang, X.; Suo, J. New progress of Keggin and Wells–Dawson type polyoxometalates catalyze acid and oxidative reactions. *J. Mol. Catal. A Chem.* **2007**, *262*, 67–76. [[CrossRef](#)]
31. Freire, C.; Fernandes, D.M.; Nunes, M.; Abdelkader, V.K. POM & MOF-based Electrocatalysts for Energy-related Reactions. *ChemCatChem* **2018**, *10*, 1703–1730.

32. Dolbecq, A.; Mialane, P.; Keita, B.; Nadjó, L. Polyoxometalate-based materials for efficient solar and visible light harvesting: Application to the photocatalytic degradation of azo dyes. *J. Mater. Chem.* **2012**, *22*, 24509–24521. [CrossRef]
33. Fernandes, D.M.; Araujo, M.P.; Haider, A.; Mougharbel, A.S.; Fernandes, A.J.S.; Kortz, U.; Freire, C. Polyoxometalate-graphene Electrocatalysts for the Hydrogen Evolution Reaction. *ChemElectroChem* **2018**, *5*, 273–283. [CrossRef]
34. Xie, X.; Nie, Y.; Chen, S.; Ding, W.; Qi, X.; Li, L.; Wei, Z. A catalyst superior to carbon-supported-platinum for promotion of the oxygen reduction reaction: Reduced-polyoxometalate supported palladium. *J. Mater. Chem. A* **2015**, *3*, 13962–13969. [CrossRef]
35. Teillout, A.-L.; de Oliveira, P.; Marrot, J.; Howell, R.; Vilà, N.; Walcarius, A.; Mbomekallé, I. Synthesis, Crystal Structure, Electrochemistry and Electro-Catalytic Properties of the Manganese-Containing Polyoxotungstate, $[(\text{Mn}(\text{H}_2\text{O})_3)_2(\text{H}_2\text{W}_{12}\text{O}_{42})]^{6-}$. *Inorganics* **2019**, *7*, 15. [CrossRef]
36. Liang, Y.Y.; Wang, H.L.; Zhou, J.G.; Li, Y.G.; Wang, J.; Regier, T.; Dai, H.J. Covalent Hybrid of Spinel Manganese-Cobalt Oxide and Graphene as Advanced Oxygen Reduction Electrocatalysts. *J. Am. Chem. Soc.* **2012**, *134*, 3517–3523. [CrossRef]
37. Ji, Y.; Huang, L.; Hu, J.; Streb, C.; Song, Y.-F. Polyoxometalate-functionalized nanocarbon materials for energy conversion, energy storage and sensor systems. *Energy Environ. Sci.* **2015**, *8*, 776–789. [CrossRef]
38. Toma, F.M.; Sartorel, A.; Iurlo, M.; Carraro, M.; Rapino, S.; Hooper-Burkhardt, L.; Da Ros, T.; Marcaccio, M.; Scorrano, G.; Paolucci, F.; et al. Tailored functionalization of carbon nanotubes for electrocatalytic water splitting and sustainable energy applications. *ChemSusChem* **2011**, *4*, 1447–1451. [CrossRef]
39. Wu, J.; Liao, L.; Yan, W.; Xue, Y.; Sun, Y.; Yan, X.; Chen, Y.; Xie, Y. Polyoxometalates immobilized in ordered mesoporous carbon nitride as highly efficient water oxidation catalysts. *ChemSusChem* **2012**, *5*, 1207–1212. [CrossRef]
40. Guo, S.-X.; Liu, Y.; Lee, C.-Y.; Bond, A.M.; Zhang, J.; Geletii, Y.V.; Hill, C.L. Graphene-supported $[(\text{Ru}_4\text{O}_4(\text{OH})_2(\text{H}_2\text{O})_4)(\gamma\text{-SiW}_{10}\text{O}_{36})_2]^{10-}$ for highly efficient electrocatalytic water oxidation. *Energy Environ. Sci.* **2013**, *6*, 2654–2663. [CrossRef]
41. Gong, R.H.; Gao, D.D.; Liu, R.J.; Sorsche, D.; Biskupek, J.; Kaiser, U.; Rau, S.; Streb, C. Self-Activation of a Polyoxometalate-Derived Composite Electrocatalyst for the Oxygen Evolution Reaction. *ACS Appl. Energy Mater.* **2021**, *4*, 12671–12676. [CrossRef]
42. Mbomekalle, I.M.; Keita, B.; Nadjó, L.; Berthet, P.; Hardcastle, K.I.; Hill, C.L.; Anderson, T.M. Multi-iron tungstodiarisenes. Synthesis, characterization, and electrocatalytic studies of alpha beta beta alpha-($\text{Fe}^{\text{III}}\text{OH}_2$) $_2\text{Fe}^{\text{III}}_2(\text{AS}_2\text{W}_{15}\text{O}_{56})_2^{12-}$. *Inorg. Chem.* **2003**, *42*, 1163–1169. [CrossRef] [PubMed]
43. Mbomekalle, I.M.; Mialane, P.; Dolbecq, A.; Marrot, J.; Secheresse, F.; Berthet, P.; Keita, B.; Nadjó, L. Rational Synthesis, Structure, Magnetism and Electrochemistry of Mixed Iron-Nickel-Containing Wells-Dawson-Fragment-Based Sandwich-Type Polyoxometalates. *Eur. J. Inorg. Chem.* **2009**, *34*, 5194–5204. [CrossRef]
44. Gomezgarcia, C.J.; Borrassalmenar, J.J.; Coronado, E.; Ouahab, L. Single-Crystal X-Ray Structure and Magnetic-Properties of the Polyoxotungstate Complexes $\text{NA}16\text{M}_4(\text{H}_2\text{O})_2(\text{P}_2\text{W}_{15}\text{O}_{56})_2$ Center-Dot- NH_2O (M=MN-II, N=53, M=NI-II, N=52)—An Antiferromagnetic MN-II Tetramer and a Ferromagnetic NI-II Tetramer. *Inorg. Chem.* **1994**, *33*, 4016–4022. [CrossRef]
45. Huang, M.C.; Teng, H.S. Nitrogen-containing carbons from phenol-formaldehyde resins and their catalytic activity in NO reduction with NH_3 . *Carbon* **2003**, *41*, 951–957. [CrossRef]
46. Kapteijn, F.; Moulijn, J.A.; Matzner, S.; Boehm, H.P. The development of nitrogen functionality in model chars during gasification in CO_2 and O_2 . *Carbon* **1999**, *37*, 1143–1150. [CrossRef]
47. Shao, Y.Y.; Zhang, S.; Engelhard, M.H.; Li, G.S.; Shao, G.C.; Wang, Y.; Liu, J.; Aksay, I.A.; Lin, Y.H. Nitrogen-doped graphene and its electrochemical applications. *J. Mater. Chem.* **2010**, *20*, 7491–7496. [CrossRef]
48. Kovtun, A.; Jones, D.; Dell’Elce, S.; Treossi, E.; Liscio, A.; Palermo, V. Accurate chemical analysis of oxygenated graphene-based materials using X-ray photoelectron spectroscopy. *Carbon* **2019**, *143*, 268–275. [CrossRef]
49. Botas, C.; Alvarez, P.; Blanco, C.; Gutierrez, M.D.; Ares, P.; Zamani, R.; Arbiol, J.; Morante, J.R.; Menendez, R. Tailored graphene materials by chemical reduction of graphene oxides of different atomic structure. *RSC Adv.* **2012**, *2*, 9643–9650. [CrossRef]
50. Tang, L.B.; Li, X.M.; Ji, R.B.; Teng, K.S.; Tai, G.; Ye, J.; Wei, C.S.; Lau, S.P. Bottom-up synthesis of large-scale graphene oxide nanosheets. *J. Mater. Chem.* **2012**, *22*, 5676–5683. [CrossRef]
51. Daems, N.; Sheng, X.; Vankelecom, I.F.J.; Pescarmona, P.P. Metal-free doped carbon materials as electrocatalysts for the oxygen reduction reaction. *J. Mater. Chem. A* **2014**, *2*, 4085–4110. [CrossRef]
52. Zhou, X.J.; Qiao, J.L.; Yang, L.; Zhang, J.J. A Review of Graphene-Based Nanostructural Materials for Both Catalyst Supports and Metal-Free Catalysts in PEM Fuel Cell Oxygen Reduction Reactions. *Adv. Energy Mater.* **2014**, *4*, 25. [CrossRef]
53. Mathumba, P.; Fernandes, D.M.; Matos, R.; Iwuoha, E.I.; Freire, C. Metal Oxide (Co_3O_4 and Mn_3O_4) Impregnation into S, N-doped Graphene for Oxygen Reduction Reaction (ORR). *Materials* **2020**, *13*, 1562. [CrossRef] [PubMed]
54. Abdelkader-Fernandez, V.K.; Fernandes, D.M.; Balula, S.S.; Cunha-Silva, L.; Freire, C. Advanced framework-modified POM@ZIF-67 nanocomposites as enhanced oxygen evolution reaction electrocatalysts. *J. Mater. Chem. A* **2020**, *8*, 13509–13521. [CrossRef]
55. Lyu, H.H.; Gao, B.; He, F.; Ding, C.; Tang, J.C.; Crittenden, J.C. Ball-Milled Carbon Nanomaterials for Energy and Environmental Applications. *ACS Sustain. Chem. Eng.* **2017**, *5*, 9568–9585. [CrossRef]
56. Liu, S.W.; Tong, M.Y.; Liu, G.Q.; Zhang, X.; Wang, Z.M.; Wang, G.Z.; Cai, W.P.; Zhang, H.M.; Zhao, H.J. S, N-Containing Co-MOF derived Co_9S_8 @S,N-doped carbon materials as efficient oxygen electrocatalysts and supercapacitor electrode materials. *Inorg. Chem. Front.* **2017**, *4*, 491–498. [CrossRef]
57. Suen, N.T.; Hung, S.F.; Quan, Q.; Zhang, N.; Xu, Y.J.; Chen, H.M. Electrocatalysis for the oxygen evolution reaction: Recent development and future perspectives. *Chem. Soc. Rev.* **2017**, *46*, 337–365. [CrossRef]

58. Frydendal, R.; Paoli, E.A.; Knudsen, B.P.; Wickman, B.; Malacrida, P.; Stephens, I.E.L.; Chorkendorff, I. Benchmarking the Stability of Oxygen Evolution Reaction Catalysts: The Importance of Monitoring Mass Losses. *ChemElectroChem* **2014**, *1*, 2075–2081. [[CrossRef](#)]
59. Soriano-Lopez, J.; Goberna-Ferron, S.; Vigarà, L.; Carbo, J.J.; Poblet, J.M.; Galan-Mascaros, J.R. Cobalt Polyoxometalates as Heterogeneous Water Oxidation Catalysts. *Inorg. Chem.* **2013**, *52*, 4753–4755. [[CrossRef](#)]
60. Soriano-Lopez, J.; Musaev, D.G.; Hill, C.L.; Galan-Mascaros, J.R.; Carbo, J.J.; Poblet, J.M. Tetracobalt-polyoxometalate catalysts for water oxidation: Key mechanistic details. *J. Catal.* **2017**, *350*, 56–63. [[CrossRef](#)]
61. Haider, A.; Bassil, B.S.; Soriano-Lopez, J.; Qasim, H.M.; de Pípaon, C.S.; Ibrahim, M.; Dutta, D.; Koo, Y.S.; Carbo, J.J.; Poblet, J.M.; et al. 9-Cobalt(II)-Containing 27-Tungsto-3-germanate(IV): Synthesis, Structure, Computational Modeling, and Heterogeneous Water Oxidation Catalysis. *Inorg. Chem.* **2019**, *58*, 11308–11316. [[CrossRef](#)] [[PubMed](#)]
62. Stracke, J.J.; Finke, R.G. Water Oxidation Catalysis Beginning with $2.5 \mu\text{M} [\text{Co}_4(\text{H}_2\text{O})_2(\text{PW}_9\text{O}_{34})_2]^{10-}$: Investigation of the True Electrochemically Driven Catalyst at $\geq 600 \text{ mV}$ Overpotential at a Glassy Carbon Electrode. *ACS Catal.* **2013**, *3*, 1209–1219. [[CrossRef](#)]
63. Zhang, C.X.; Wu, C.; Gao, Y.; Gong, Y.; Liu, H.Y.; He, J.P. FeNi Nanoparticles Coated on N-doped Ultrathin Graphene-like Nanosheets as Stable Bifunctional Catalyst for Zn-Air Batteries. *Chem. Asian J.* **2021**, *16*, 1592–1602. [[CrossRef](#)]
64. Battiato, S.; Urso, M.; Cosentino, S.; Pellegrino, A.L.; Mirabella, S.; Terrasi, A. Optimization of Oxygen Evolution Reaction with Electroless Deposited Ni-P Catalytic Nanocoating. *Nanomaterials* **2021**, *11*, 3010. [[CrossRef](#)] [[PubMed](#)]
65. Liu, Y.Y.; Jiang, H.L.; Zhu, Y.H.; Yang, X.L.; Li, C.Z. Transition metals (Fe, Co, and Ni) encapsulated in nitrogen-doped carbon nanotubes as bi-functional catalysts for oxygen electrode reactions. *J. Mater. Chem. A* **2016**, *4*, 1694–1701. [[CrossRef](#)]
66. Zhang, J.W.; Zhang, H.; Ren, T.Z.; Yuan, Z.Y.; Bandosz, T.J. FeNi doped porous carbon as an efficient catalyst for oxygen evolution reaction. *Front. Chem. Sci. Eng.* **2021**, *15*, 279–287. [[CrossRef](#)]
67. Song, F.; Hu, X.L. Exfoliation of layered double hydroxides for enhanced oxygen evolution catalysis. *Nat. Commun.* **2014**, *5*, 4477. [[CrossRef](#)]
68. Zhang, X.; Xu, H.M.; Li, X.X.; Li, Y.Y.; Yang, T.B.; Liang, Y.Y. Facile Synthesis of Nickel-Iron/Nanocarbon Hybrids as Advanced Electrocatalysts for Efficient Water Splitting. *ACS Catal.* **2016**, *6*, 580–588. [[CrossRef](#)]
69. Lee, G.Y.; Kim, I.; Lim, J.; Yang, M.Y.; Choi, D.S.; Gu, Y.; Oh, Y.; Kang, S.H.; Nam, Y.S.; Kim, S.O. Spontaneous linker-free binding of polyoxometalates on nitrogen-doped carbon nanotubes for efficient water oxidation. *J. Mater. Chem. A* **2017**, *5*, 1941–1947. [[CrossRef](#)]
70. Abdelkader-Fernandez, V.K.; Fernandes, D.M.; Cunha-Silva, L.; Fernandes, A.J.S.; Freire, C. Decorating MOF-74-derived nanocarbons with a sandwich-type polyoxometalate to enhance their OER activity: Exploring the underestimated bulk-deposition approach. *Electrochim. Acta* **2021**, *389*, 138719. [[CrossRef](#)]
71. Wang, Y.; Wang, Y.Y.; Zhang, L.; Liu, C.S.; Pang, H. Core-shell-type ZIF-8@ZIF-67@POM hybrids as efficient electrocatalysts for the oxygen evolution reaction. *Inorg. Chem. Front.* **2019**, *6*, 2514–2520. [[CrossRef](#)]
72. Imani, A.H.; Ojani, R.; Raoof, J.B. Novel polyoxometalate-based composite as efficient electrocatalyst for alkaline water oxidation reaction. *J. Iran. Chem. Soc.* **2021**, *18*, 2079–2089. [[CrossRef](#)]
73. Zhang, L.; Mi, T.; Ziaee, M.A.; Liang, L.; Wang, R. Hollow POM@MOF hybrid-derived porous $\text{Co}_3\text{O}_4/\text{CoMoO}_4$ nanocages for enhanced electrocatalytic water oxidation. *J. Mater. Chem. A* **2018**, *6*, 1639–1647. [[CrossRef](#)]
74. Huang, Z.; Yang, Z.; Hussain, M.Z.; Chen, B.; Jia, Q.; Zhu, Y.; Xia, Y. Polyoxometallates@zeolitic-imidazolate-framework derived bimetallic tungsten-cobalt sulfide/porous carbon nanocomposites as efficient bifunctional electrocatalysts for hydrogen and oxygen evolution. *Electrochim. Acta* **2020**, *330*, 135335. [[CrossRef](#)]
75. Tao, Z.; Wang, T.; Wang, X.; Zheng, J.; Li, X. MOF-Derived Noble Metal Free Catalysts for Electrochemical Water Splitting. *ACS Appl. Mater. Interfaces* **2016**, *8*, 35390–35397. [[CrossRef](#)] [[PubMed](#)]
76. Xie, C.; Wang, Y.; Hu, K.; Tao, L.; Huang, X.; Huo, J.; Wang, S. In situ confined synthesis of molybdenum oxide decorated nickel-iron alloy nanosheets from MoO_4^{2-} intercalated layered double hydroxides for the oxygen evolution reaction. *J. Mater. Chem. A* **2017**, *5*, 87–91. [[CrossRef](#)]
77. Li, Y.; He, H.; Fu, W.; Mu, C.; Tang, X.Z.; Liu, Z.; Chi, D.; Hu, X. In-grown structure of NiFe mixed metal oxides and CNT hybrid catalysts for oxygen evolution reaction. *Chem. Commun.* **2016**, *52*, 1439–1442. [[CrossRef](#)]